Journal of
Materials Chemistry A

PAPER

Cite this: *J. Mater. Chem. A*, 2017, **5**, 2629

Three-dimensional tetsubo-like $Co(OH)_2$ nanorods on a macroporous electrically conductive network as an efficient electroactive framework for the hydrogen evolution reaction

Xin Tong,[ab] Dajun Wu,[b] Chi Zhang,[b] Kenan Lian,[b] Dayuan Xiong,*[a] Shaohui Xu,[b] Yiping Zhu,[b] Ruijuan Qi,[b] Rong Huang,[b] Lianwei Wang*[abc] and Paul K. Chu[c]

Received 10th November 2016
Accepted 22nd December 2016

DOI: 10.1039/c6ta09728f

www.rsc.org/MaterialsA

Conducting the hydrogen evolution reaction (HER) in an alkaline environment using a non-precious transition metal catalyst with high efficiency is challenging. Here, we report excellent HER activity achieved using three-dimensional (3D) tetsubo-like $Co(OH)_2$ nanorods on a macroporous electrically conductive network (MECN) synthesized by a hydrothermal method. This unique framework comprises three levels of porous structures, including a bottom-ordered MECN substrate, an intermediate layer of vertically porous $Co(OH)_2$ nanowires with a mean diameter of 100 nm and length of about 2 μm, and outmost $Co(OH)_2$ nanosheets (≈20 nm). The 3D array structure with a large aspect ratio provides a large specific surface area and exposes more active sites to catalyze electrochemical reactions at the electrode–electrolyte interface. Compared with $Co(OH)_2$ nanosheets on an MECN and foamy $Co(OH)_2$ on an MECN structure, the synthesized architecture has excellent HER catalytic reactivity, including a low potential of −69.2 mV *vs.* RHE, a cathodic current density of 10 mA cm^{-2}, a small Tafel slope of 61.9 mV dec^{-1}, a high current density, and robust catalytic stability in 1 M KOH, and is promising in HER applications.

1 Introduction

Owing to increasing energy demands and concerns regarding environmental impact, much effort has been made to develop and utilize renewable energy and associated techniques to minimize the use of fossil fuels.[1,2] In energy conversion technologies such as electrochemical water splitting, cost-effective active catalytic materials are key.[3–5] The hydrogen evolution reaction (HER), which is a half reaction in water splitting, may fulfill the energy requirements.[6] Although platinum (Pt) is the most efficient HER catalyst, its high cost limits its large-scale application.[7,8] In this respect, transition metal compounds are potential catalysts for the HER because of their low cost and environmental friendliness.[9–15] Nonetheless, it is important to identify economical non-precious transition metal compounds with efficient electrocatalytic properties.[16] To date, the catalytic performance of a number of different materials has been studied,[17,61] for example, transition metal chalcogenide ($NiCo_2S_4$) nanowires (NWs)/Ni foam (NF), MoS_2 nanosheets (NSs),[18,19] carbides (VC NSs, Mo_2C),[20,21] nitrides (WN nanoparticles, Mo_2N),[22,23,62] phosphides (FeP NWs, Ni_2P, CoP nanocrystals, *etc.*),[24–26] oxides (Co/Co_3O_4 core/shell NSs, $NiCo_2O$/CNTs),[27,28] and transition-metal hydroxides such as nickel hydroxide and cobalt hydroxides.[29,30] In particular, $Co(OH)_2$ is promising due to its low cost, environmental friendliness, and high catalytic activity.[31] There have been efforts to synthesize $Co(OH)_2$ structures with different morphologies, including nanoparticles, nanocones, nanowires, and nanosheets.[32–35] For example, Feng *et al.* prepared $Co(OH)_2$@PANI hybrid nanosheets with a 3D network with good electrocatalytic HER activity in 1 M KOH.[35] In another study, CoS-doped β-$Co(OH)_2$@-amorphous MoS_{2+x} hybrid catalysts grown on nickel foam and synthesized in a one-step reaction showed a HER current density of 10 mA cm^{-2} at an overpotential of 143 mV in 1.0 M KOH.[34]

In general, high catalytic performance stems from synergistic effects rendered by the electroactive materials and the substrate.[35] Nanostructured cobalt hydroxide has been fabricated on different substrates such as Ni foam,[36] graphene composites,[37] carbon nitride,[38] Ag nanowires,[39] and carbon fibers.[40] However, owing to the disordered structure of these electrocatalysts, some of the internal electrocatalytic sites cannot be fully utilized, resulting in low electrocatalytic activity in the HER.[41] It is thus necessary to optimize the structure of the catalysts to improve the

---

[a] *Shanghai Key Laboratory of Multidimensional Information Processing, East China Normal University, 500 Dongchuan Road, Shanghai 200241, P. R. China. E-mail: dyxiong@ee.ecnu.edu.cn; lwwang@ee.ecnu.edu.cn; Fax: +86-021-54345119; Tel: +86-021-54345200; +86-021-54345160*

[b] *Key Laboratory of Polar Materials and Devices, Ministry of Education, Department of Electronic Engineering, East China Normal University, 500 Dongchuan Road, Shanghai 200241, P. R. China*

[c] *Department of Physics and Material Science, City University of Hong Kong, Tat Chee Avenue, Kowloon, Hong Kong, China*

HER efficiency.[63,64] A new trend is to produce a structure with a large surface area, porous nanostructure, and good adhesion on a three-dimensional (3D) ordered substrate with a large surface-to-volume ratio.[42,43] Although we have fabricated $Co(OH)_2$ nanosheets on MECNs as supercapacitors by electrochemical deposition or hydrothermally,[44–46] 3D tetsubo-like $Co(OH)_2$ nanorods have never been prepared on a macroporous electrically conductive network (MECN).

In this work, tetsubo-like $Co(OH)_2$ nanorods are produced on a MECN (tetsubo-like $Co(OH)_2$ NRs/MECN) with a large aspect ratio by a pressurized hydrothermal method and the HER properties in an alkaline environment are investigated. The $Co(OH)_2$ nanosheets (NSs) are produced on $Co(OH)_2$ nanowires (NWs) as a tetsubo-like $Co(OH)_2$ NR nanostructure, which provides a large interfacial area and ample active sites. The SEM and TEM images of the tetsubo-like $Co(OH)_2$ NRs/MECN show that the structure possesses a special nanostructure composed of nanosheets with an average thickness of 20 nm and nanowires with an average diameter of 100 nm and length of around 2 μm. X-ray spectra, including X-ray diffraction and X-ray photoelectron spectroscopy spectra, demonstrate the crystalline phase structure and valence of the tetsubo-like $Co(OH)_2$ NRs/MECN. In addition, the tetsubo-like $Co(OH)_2$ NRs/MECN shows a low overpotential of −69.2 mV *vs.* RHE at a current density of 10 mA cm^{-2} and a Tafel slope of 61.9 mV dec^{-1} in the HER in 1 M KOH, and the performance of the structure is superior to that observed for pristine MECNs, $Co(OH)_2$ NSs/MECNs, and foamy $Co(OH)_2$/MECNs.

2 Experimental details

2.1 Chemicals and substrates

All chemicals were of analytical grade and used without purification. Nickel chloride ($NiCl_2\cdot6H_2O$) and ammonium chloride (NH_4Cl) were obtained from Aladdin Reagent. Sodium hypophosphite ($NaH_2PO_2\cdot H_2O$), ammonia (NH_4OH), cobaltous nitrate hexahydrate ($Co(NO_3)_2\cdot6H_2O$) and carbamide ($CO(NH_2)_2$) were purchased from Sinopharm Chemical Reagent Co. Ltd. Aqueous solutions were prepared with 18 MΩ deionized water at room temperature. The Si microchannel plates (Si-MCPs) were fabricated by electrochemical etching[47] and divided into 1 cm × 1 cm samples by laser cutting.[48]

2.2 Preparation of the MECN

The macroporous electrically conductive network (MECN) was prepared by electroless plating of Si microchannel plates (Si-MCPs) as described previously.[49] The Si-MCP comprised a square array of 5 μm × 5 μm pore array channels about 250 μm in depth and 1 μm thickness of the wall. The nickel layer was deposited on the outer surface and inner sidewalls of the Si-MCPs simultaneously. In order to decrease the electrical resistivity, the porous nano-Ni was produced by a drop flowing deposition method.[44] 5.0 g of NH_4Cl (complexing agent) and 1.2 g of $NaH_2PO_2\cdot H_2O$ (reducing agent) were dissolved in 90 mL of 24 mM $NiCl_2\cdot6H_2O$ to form a green mixture. The pH of the solution was adjusted to 9–11 using NH_4OH, and the solution was stirred for 30 min. The Si-MCPs were immersed in a HF solution ($HF : C_2H_5OH : H_2O$, 100 : 125 : 10, v/v) for 5 min to remove impurities, then transferred to the electroless plating solution, stirred magnetically for 20 min at 90 °C in a liquid flow instrument, and dried at 80 °C overnight under vacuum. The reactions are:

$$H_2PO_2^- + 3OH^- \rightarrow HPO_3^{2-} + 2H_2O + 2e^- \quad (1)$$

$$Ni^{2+} + 2e^- \rightarrow Ni \quad (2)$$

2.3 Synthesis of tetsubo-like $Co(OH)_2$ nanorods on the MECN

A 1.5 mM cobalt nitrate solution was prepared with DI water (50 mL), 7.5 mmol of urea was added as a reducing agent, and then the mixture was stirred for 5 min to obtain a clear solution. The solution was then transferred to a Teflon-lined stainless-steel autoclave. For *in situ* growth of the catalyst, the MECN was transferred to a buffer solution of Triton X-100 for at least 2 minutes to increase the hydrophilicity, and the surface-cleaned MECN was then immersed in the cobalt nitrate solution. The autoclave was locked tightly and maintained at 150 °C for 3 h in a vacuum oven. After a certain period, the uniform tetsubo-like $Co(OH)_2$ nanorod arrays on the MECN were removed from the solution, washed several times with DI water to remove unreacted residues and dried at 80 °C under vacuum for 6 h. To compare the catalytic activity, $Co(OH)_2$ nanosheets and foamy $Co(OH)_2$ were also prepared on the MECN by the same method, but with different hydrothermal treatment times (2 h and 4 h).

2.4 Material characterization

The microstructure, morphology, and size of the samples were investigated by field-emission scanning electron microscopy (FE-SEM, Hitachi S-4800, Japan). HR-TEM (JEM-2010F, JEOL) was performed at 200 kV and the phase composition was determined by X-ray diffraction (XRD, Rigaku, RINR2000, Japan) with Cu K_α radiation ($\lambda = 1.5406$ Å). The chemical composition was determined by X-ray photoelectron spectroscopy (XPS, AXIS ULTRA DLD XPS). The Raman scattering spectra were acquired from 0 to 3000 cm^{-1} on a micro-Raman instrument (T6400 Jobin Yvon triple monochromator, Tokyo, Japan) equipped with a charge-coupled detector and an Ar laser (633 nm).

2.5 Electrochemical measurements

The catalytic properties were determined using a three-electrode setup on a CHI 660E electrochemical workstation (Chenhua Instruments, Shanghai) at room temperature. The MECN, 2 h $Co(OH)_2$/MECN, 3 h $Co(OH)_2$/MECN, and 4 h $Co(OH)_2$/MECN served separately as the working electrodes, and a saturated calomel electrode (SCE) and Pt foil were used as the reference and counter electrodes, respectively. The measurements were performed in 150 mL of 1 M KOH (pH = 13.6) prepared with 18 MΩ DI water. The performance of the hydrogen evolution catalyst was assessed by linear sweep voltammetry from −0.43 V to 0.2 V *vs.* RHE at a scanning rate of 5 mV s^{-1}. The Tafel plots were obtained from the potentiodynamic polarization tests conducted at sweeping rates of 1 mV s^{-1} in the anodic direction. Electrochemical impedance spectroscopy (EIS) was performed with the working electrode without a bias or biased at a certain potential, while the frequency was swept from 100 kHz to 0.01 Hz. All of the potentials were determined with respect to RHE using the following equation:[50] $E_{\mathrm{RHE}} = E_{\mathrm{SCE}} + 0.0592 \times \mathrm{pH} + 0.2415$. The overpotential ($\eta$) of the HER was then obtained from[51] $\eta_{\mathrm{HER}} = -E_{\mathrm{RHE}}$.

3 Results and discussion

3.1 Characterization of the $Co(OH)_2$/MECN catalyst

The top-view and cross-sectional morphologies of the Si-MCPs and Ni/Si-MCPs (MECN) before and after plating were examined by SEM. As shown in Fig. 1(a)–(d), before plating, the microchannels had a depth of about 250 μm and a size of 5 × 5 μm, giving an aspect ratio of around 50. Electroless deposition[49] of Ni was carried out on the Si-MCPs with a low resistance of less than 1 Ω for 20 min. The uniform deposition of nickel onto the sidewalls of the microchannels was facilitated by the abundance of nanoparticles on the sidewalls; this is beneficial for the further deposition of active substances on the inner sidewalls of the Ni/Si-MCPs and provides good protection of the silicon backbone in the KOH electrolyte. Fig. 2 displays a schematic illustration of the *in situ* growth of the tetsubo-like $Co(OH)_2$ nanorod arrays on the 3D electrically conducting MECN by a one-step hydrothermal method. The MECN is selected as the substrate because of its excellent electrical conductivity, and large-aspect-ratio 3D microchannel array structure (Fig. 2(a)). In the first step, uniform $Co(OH)_2$ nanosheets are produced on the MECN (1 cm × 1 cm) by hydrothermal treatment of Co^{2+} in water in the presence of urea at 150 °C for 2 h (Fig. 2(b)). The $Co(OH)_2$ nanowires are formed during a 2.5 h period (Fig. 2(c)) and then converted into tetsubo-like nanorods (Fig. 2(d)) over a period of 3 h by a hydrothermal method, with the MECN serving as the skeleton to anchor the nanorods. The sample surface is completely covered with the tetsubo-like $Co(OH)_2$ nanorods, and FE-SEM confirms the formation of the nanorod arrays on the 3D structure (Fig. 2(d)). As is well known, the use of different synthesis times can affect the external structure, and the crystal growth mechanisms in solution are so complicated that the actual crystallization mechanism remains an open question. Initial nucleation, oriented aggregation, and Ostwald ripening, *etc.*, have been suggested to account for the process of crystal growth.[65] $Co(NO_3)_2$, H_2O and $CO(NH_2)_2$ react with each other to form $Co(OH)_2$. The reactions[52] are described as follows:

$$NO_3^- + 7H_2O + 8e^- \rightarrow NH_4^+ + 10OH^- \qquad (3)$$

$$Co^{2+} + 2OH^- \rightarrow Co(OH)_2 \qquad (4)$$

Subsequently, the nanoparticles begin to assemble together and spontaneously aggregate into $Co(OH)_2$ nanosheet structures.[65] Due to a reduction in the high surface energy through the process known as oriented aggregation, $Co(OH)_2$ nanowires

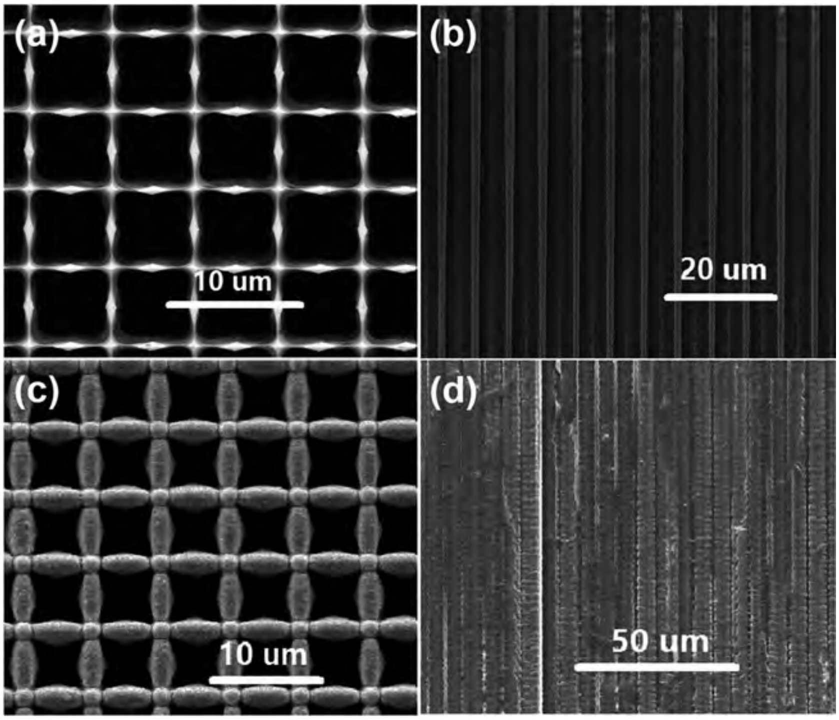

Fig. 1 (a) Top view of the Si-MCPs, (b) cross-sectional morphology of the Si-MCPs, (c) top view of the MECN, and (d) cross-sectional morphology of the MECN.

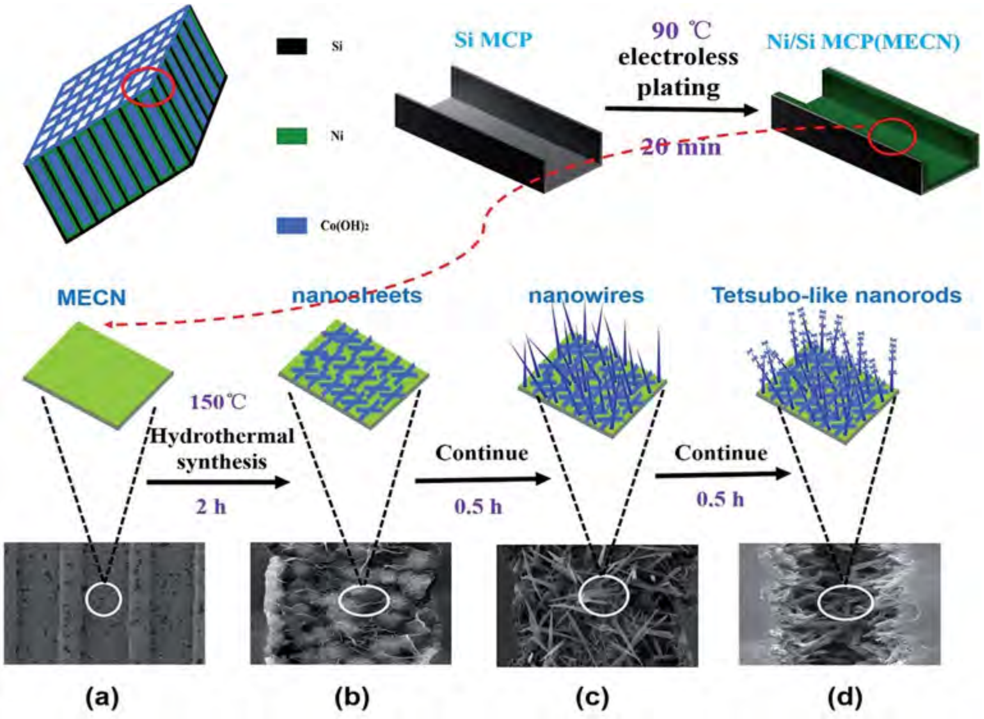

Fig. 2 Schematic illustration of the formation of tetsubo-like $Co(OH)_2$ nanorods on MECN and the corresponding cross-sectional morphology: (a) MECN, (b) *in situ* growth of $Co(OH)_2$ nanosheets on MECN (2 h), (c) *in situ* growth of $Co(OH)_2$ nanowires on MECN (2.5 h), and (d) *in situ* growth of tetsubo-like $Co(OH)_2$ nanorods on MECN (3 h).

are formed.[66] Ostwald ripening dictates the rate of growth and recrystallization, and the $Co(OH)_2$ nanowires are finally converted into tetsubo-like nanorods through an Ostwald ripening process.[67]

The morphology of the 3D $Co(OH)_2$/MECNs was examined by SEM and TEM. Fig. 3 displays the FE-SEM images of the catalysts on the MECN support. The top-view and cross-sectional morphologies of the $Co(OH)_2$/MECNs (2 h) are shown in

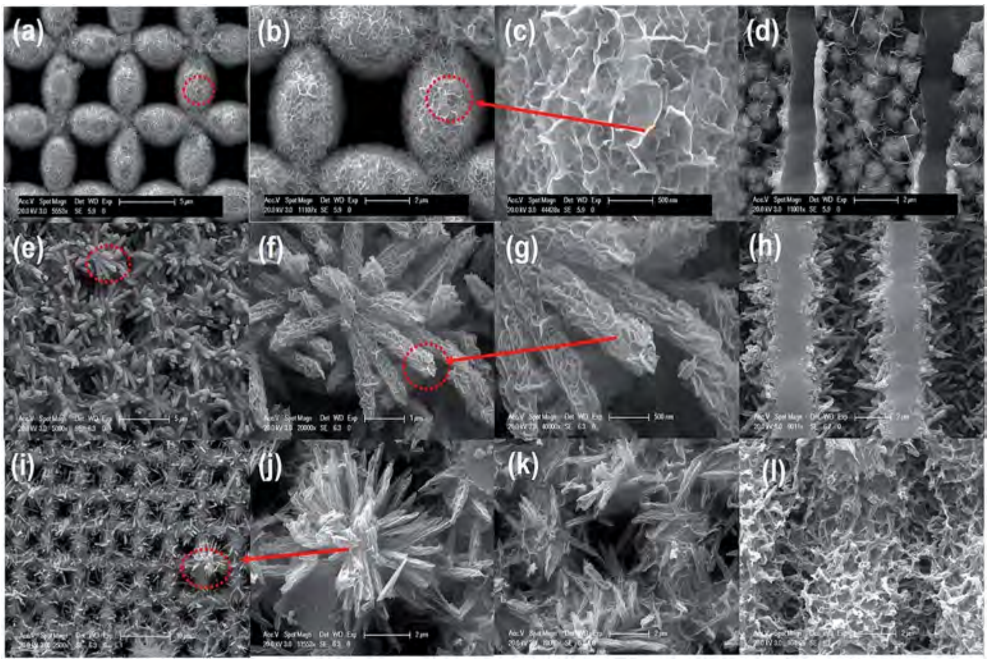

Fig. 3 (a)–(c) Top view of the $Co(OH)_2$/MECN (2 h) at different magnifications; (d) cross-sectional morphology of $Co(OH)_2$/MECN (2 h); (e)–(g) top view of the $Co(OH)_2$/MECN (3 h) at different magnifications; (h) cross-sectional morphology of $Co(OH)_2$/MECN (3 h); (i)–(k) top view of the $Co(OH)_2$/MECN (4 h) at different magnifications; (l) cross-sectional morphology of $Co(OH)_2$/MECN (4 h).

Fig. 3(a)–(d). The vertical $Co(OH)_2$ nanosheets cover the inner side and surface, forming the 3D $Co(OH)_2$/MECN array structure, as shown in Fig. 3(a)–(d). The porous $Co(OH)_2$ NS network has a pore size of 0.1–0.5 μm and a thickness of about 20 nm. Fig. 3(e)–(g) show images of the tetsubo-like $Co(OH)_2$ nanorods at different magnifications. Fig. 3(e) reveals that the MECN is covered uniformly with the $Co(OH)_2$ catalyst, forming 3D porous nanorods (Fig. 3(g)), and Fig. 3(h) discloses that the tetsubo-like $Co(OH)_2$ nanorod arrays are also formed on the inner side of the MECN. The $Co(OH)_2$ nanorods have a mean diameter of about 150 nm and a length of about 2 μm. Similarly, the foamy $Co(OH)_2$ NRs (Fig. 3(i)–(l)) are uniformly distributed on the surface and inner sidewall of the MECN. The $Co(OH)_2$ NRs on the surface resemble flowers and those formed on the inner side of MECN are like foam, because of aggregation.

The TEM image of the $Co(OH)_2$ in Fig. 4(a) confirms the nanorod structure. The length of the $Co(OH)_2$ nanorods is about 2 μm and the diameter is about 150 nm, consistent with the SEM images. The high-resolution (HR) TEM image of the $Co(OH)_2$ NSs on the tetsubo-like $Co(OH)_2$ NRs in Fig. 4(b) shows that $Co(OH)_2$ has an obvious lattice fringe indicative of a crystalline structure. The interplanar spacing in Fig. 4(b) is 0.46 nm, corresponding to the (001) lattice spacing of $Co(OH)_2$.[33,42] The HR-TEM image of the $Co(OH)_2$ NRs in Fig. 4(c) further confirms that the $Co(OH)_2$ NRs have a crystalline structure. The interplanar spacings in Fig. 4(c) are 0.27 and 0.24 nm, corresponding to the (100) and (011) lattice spacings of $Co(OH)_2$, respectively. The selected-area electron diffraction (SAED) patterns in Fig. 4(d) reveal several intense spots in random orientations arising from the crystalline structure, which is consistent with the HR-TEM images in Fig. 4(b) and (c).

To determine the chemical composition of the $Co(OH)_2$ on MECN, powder XRD and Raman scattering were conducted. As shown in Fig. 5(a), the peaks of the Si-MCPs [(400), marked with a square] with high intensities are not shown completely here. All of the samples show three distinct (111), (200) and (220) diffraction peaks (marked with a solid triangle) at $2\theta = 44.8°$, 52.3° and 76.1° (Ni: JCPDS card no. 01-089-7128). In addition to the three representative peaks from the MECN substrate, the other sharp diffraction peaks with 2θ values of 33.0° and 61.8° (marked with a solid diamond) are indexed to $Co(OH)_2$ (JCPDS 30-0443).[34] Fig. 5(b) shows the Raman spectrum of the $Co(OH)_2$/MECN composite. There is a distinct peak at 520 cm^{-1} assigned to the $Co(OH)_2$ crystalline phase. The valence states of nickel and cobalt in $Co(OH)_2$/MECN are determined by XPS. The survey spectrum in Fig. 5(c) shows the presence of C, O, Ni, Co, and Si. Comparison of the initial sample with the sample after 5000 CV cycles indicates that the Pt counter electrode does not dissolve into the solution or become deposited on the working electrode, and thus it does not contribute to the HER activity of the working electrode. As shown in Fig. 5(d), the binding energies of the Co $2p_{3/2}$ and Co $2p_{1/2}$ photoelectrons are 779.7 eV and 795.2 eV, corresponding to Co^{2+} and Co^{3+}, respectively, with an energy separation of 15.5 eV, in good agreement with reported data for Co $2p_{3/2}$ and Co $2p_{1/2}$ in $Co(OH)_2$.[53] The weak satellite peaks indicate that the majority of the Co atoms are in the Co^{3+} state.[54] Similarly, in the Ni 2p XPS spectrum (Fig. 5(e)), the binding energies at 853.2 eV for Ni $2p_{3/2}$ and 872.6 eV for Ni $2p_{1/2}$ are spin–orbit characteristics of Ni^{2+}, while the binding energies at 856.2 eV for Ni $2p_{3/2}$ and 874.4 eV for Ni $2p_{1/2}$ are spin–orbit characteristics of Ni^{3+}.[55] Likewise, the intense satellite peak suggests that Ni^{2+} is predominant.[56] The O

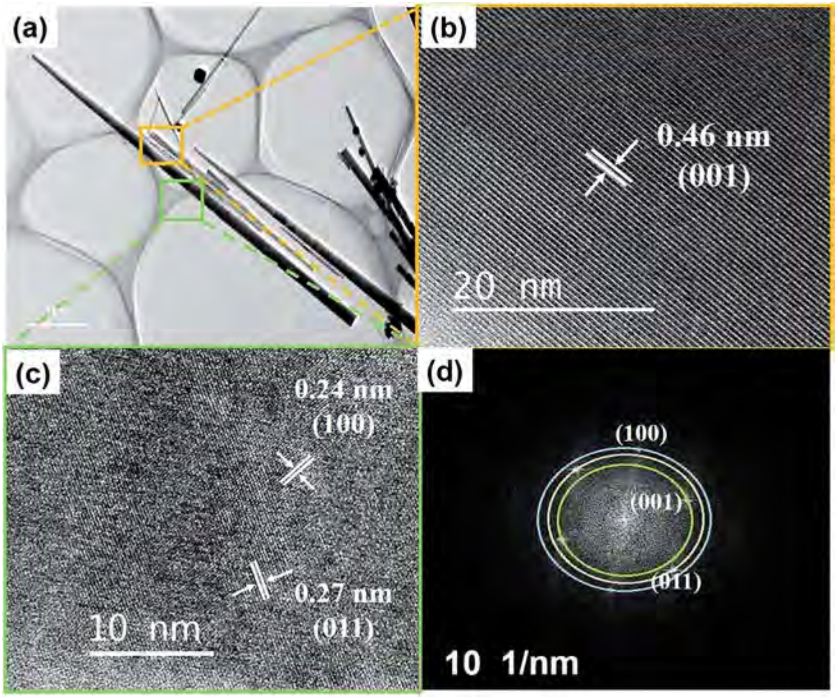

Fig. 4 (a) TEM image of $Co(OH)_2$/MECN (3 h); (b and c) HR-TEM images of $Co(OH)_2$/MECN (3 h); (d) SAED pattern.

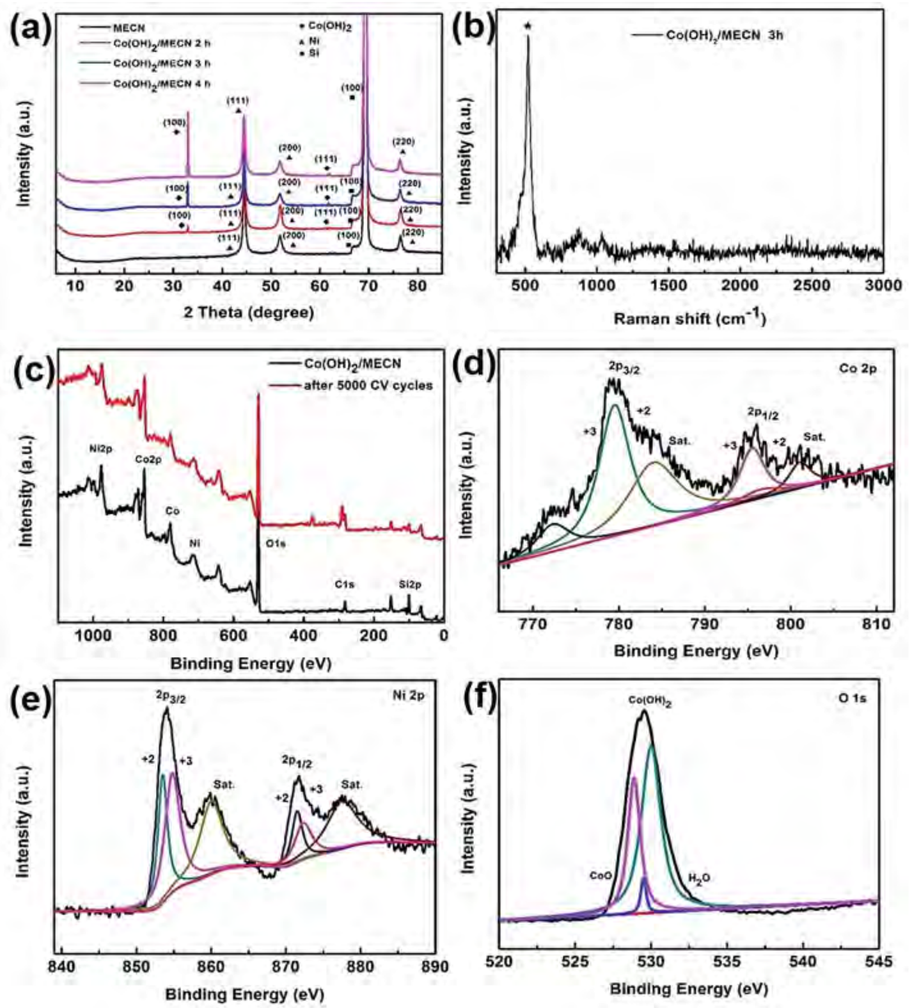

Fig. 5 (a) XRD patterns of MECN, $Co(OH)_2$/MECN (2 h), $Co(OH)_2$/MECN (3 h), and $Co(OH)_2$/MECN (4 h); (b) Raman spectra of $Co(OH)_2$/MECN; (c) XPS survey spectra of $Co(OH)_2$/MECN (3 h) before and after 5000 CV cycles; XPS spectra of (d) Co 2p, (e) Ni 2p, and (f) O 1s for $Co(OH)_2$/MECN (3 h).

1s spectrum shows three oxygen contributions denoted as O1 (528.9 eV), O2 (529.5 eV) and O3 (530.0 eV), ascribed to Co–O, Co–OH, and physisorbed/chemisorbed oxygen at/near the surface,[57] respectively. These results are in good agreement with the observed XRD patterns of the $Co(OH)_2$ on the MECN.

3.2 Electrocatalytic properties in the HER

To explore the suitability of the tetsubo-like $Co(OH)_2$ NRs/MECN catalysts in water splitting, the electrocatalytic HER performance of all of the samples was assessed in 1 M KOH using LSV in a three-electrode system. Fig. 6(a) presents the polarization curves of MECNs, $Co(OH)_2$/MECNs (2 h), $Co(OH)_2$/MECNs (3 h), $Co(OH)_2$/MECNs (4 h), and Ni foam. The cathodic current density is an important criterion in evaluating the HR activity of catalysts. With regard to $Co(OH)_2$/MECNs (3 h), only −69.3 mV is required to generate a cathodic current density of 10 mA cm^{-2}, which is much smaller than the values (−94.2 mV and −119.3 mV) required for the $Co(OH)_2$/MECNs (4 h) and $Co(OH)_2$/MECNs (2 h). The MECN requires an overpotential of 124.2 mV for a current density of 10 mA cm^{-2} and the Ni foam requires a very high overpotential of 229.7 mV to produce a current density of 10 mA cm^{-2}. The unique 3D architecture offers a large interfacial area for the reaction, numerous channels for rapid diffusion of electrolyte ions, and fast electron transport leading to excellent HER performance. Fig. 6(b) presents the overpotentials required by the electrocatalysts to give current densities of 10 mA cm^{-2} and 20 mA cm^{-2} in 1 M KOH and Fig. 6(c) displays the corresponding Tafel plots. The linear regions in the LSV curves are fitted to the Tafel equation to measure the corresponding Tafel slopes. The Tafel slope of the $Co(OH)_2$/MECNs (3 h) (61.9 mV dec^{-1}) is smaller than those of the other electrocatalysts: 83.8, 90.8, 98.9 and 110.2 mV dec^{-1} for $Co(OH)_2$/MECNs (4 h), $Co(OH)_2$/MECNs (2 h), MECNs, and Ni foam, respectively. The Tafel slope also reveals better HER performance from the $Co(OH)_2$/MECNs (3 h), in good agreement with the LSV data. A small Tafel slope is desirable in practice because of the energy efficiency and enhancement of hydrogen evolution at a small overpotential. The HER performance of the tetsubo-like $Co(OH)_2$/MECNs//$Co(OH)_2$ NSs/MECNs//foamy $Co(OH)_2$/MECNs is comparable to that recently reported for

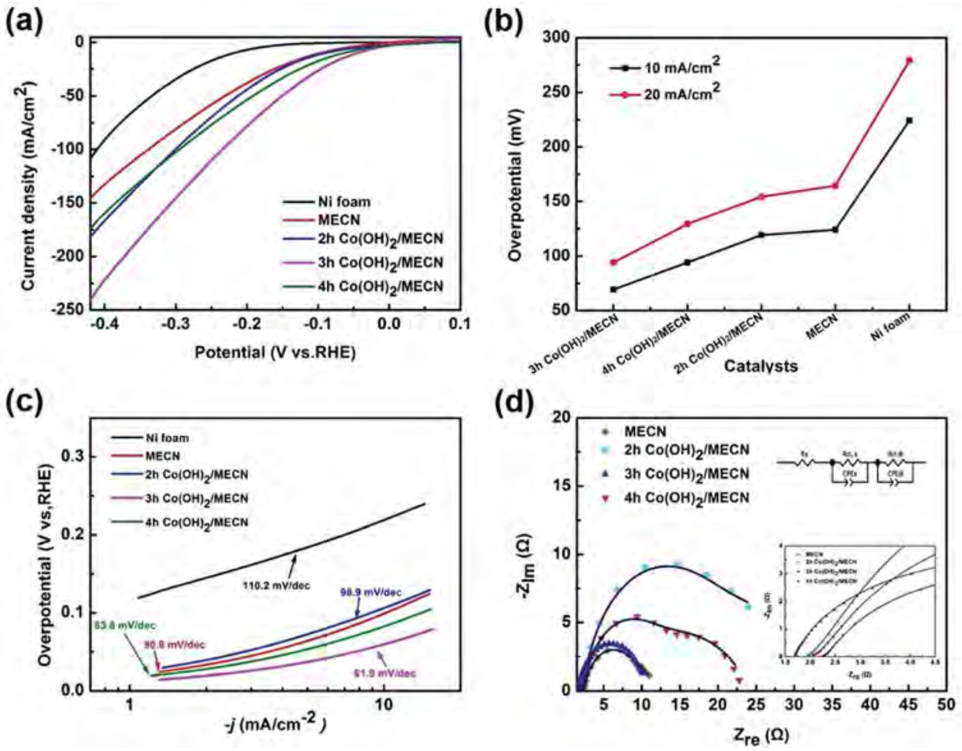

Fig. 6 (a) HER polarization curves of Ni foam, MECN, $Co(OH)_2$/MECN (2 h), $Co(OH)_2$/MECN (3 h), and $Co(OH)_2$/MECN (4 h) at a scanning rate of 5 mV s^{-1}; (b) the overpotential required to achieve a current density of 10 mA cm^{-2} and 20 mA cm^{-2} for the different electrocatalysts; (c) the corresponding Tafel plots of the HER; (d) Nyquist plots of the MECN, $Co(OH)_2$/MECN (2 h), $Co(OH)_2$/MECN (3 h), $Co(OH)_2$/MECN (4 h) electrodes for the frequency range between 100 kHz and 10 mHz in 1 M KOH.

Co-based electroactive materials (Table 1). In particular, the HER activity observed from the $Co(OH)_2$/MECNs (3 h) is excellent, due to the 3D ordered architecture, large surface area, and abundant active sites.

To elucidate the HER kinetics on the surface of the catalysts, electrochemical impedance spectroscopy (EIS) was performed. As can be seen from Fig. 6(d), the Nyquist plots are presented, in which the square, round and triangular signs represent the experimental data and the solid lines are the results fitted to an equivalent circuit shown in the inset of Fig. 6(d). In the equivalent circuit, R_s represents the overall series resistance, CPE_s is the capacitance phase element of the depletion layer, $R_{ct,s}$ is the charge transfer resistance in the depletion layer, CPE_{dl} is the capacitance phase element in the double layer at the catalyst–electrolyte interface, and $R_{ct,dl}$ is the charge transfer resistance of the double layer at the catalyst–electrolyte interface. $R_{ct,dl}$ is correlated to the kinetics of the faradaic reaction across the double layer, with a smaller value corresponding to a faster reaction rate. The high-frequency response in EIS is attributed to the charge transfer process in the depletion layer of the catalysts (*i.e.*, $Co(OH)_2$/MECN (3 h) and $Co(OH)_2$/MECN (4 h)). The low-frequency response is associated with charge transfer across the

Table 1 Comparison of HER activity data among various catalysts in the literature

Catalyst	Support	Electrolyte	η (V *vs.* RHE) for 10 mA cm^{-2}	η (V *vs.* RHE) for 20 mA cm^{-2}	Tafel slope (mV dec^{-1})	Ref.
Tetsubo-like $Co(OH)_2$ NWs	MECN	1 M KOH	69.3	94.2	61.9	This work
$Co(OH)_2$ NSs	MECN	1 M KOH	94.2	129.2	83.8	This work
Foamy $Co(OH)_2$	MECN	1 M KOH	119.3	154.5	90.8	This work
$Co(OH)_2$@PANI HNSs	Ni foam	1 M KOH	65	95	91.6	35
CoS–$Co(OH)_2$@aMoS_{2+x}	Ni foam	1 M KOH	143	175	68	34
$NiCo_2S_4$ NW	Ni foam	1 M KOH	210	275	58.9	18
Co/Co_3O_4 core/shell NSs	Ni foam	1 M KOH	90	135	44	27
CoP	Carbon cloth	0.5 M H_2SO_4	67	100	51	59
CoP	Ti foil	0.5 M H_2SO_4		85	50	60
$Co_{0.6}Mo_{1.4}N_2$	GCE	0.1 M $HClO_4$	202	267		57
Co	CNF-700	1 M KOH	196	263	96	58

Table 2 Fitted results of important parameters in the equivalent circuit

	R_s (Ω)	$R_{ct,s}$ (Ω)	$R_{ct,dl}$ (Ω)	CPE_s-T	CPE_s-P	CPE_{dl}-T	CPE_{dl}-P
MECN	2.25	5.419	5.006	0.135	0.519	0.014	0.936
2 h $Co(OH)_2$/MECN	1.936	12.76	21.91	0.014	1.004	0.076	0.562
3 h $Co(OH)_2$/MECN	1.682	7.954	4.295	0.010	0.882	0.837	0.508
4 h $Co(OH)_2$/MECN	2.048	16.15	6.089	0.056	0.563	0.009	1.026
3 h $Co(OH)_2$/MECN 5000 cycles	1.686	0.181	152	1.086	0.602	0.410	0.906

double layer at the catalyst–electrolyte interface. The $Co(OH)_2$/MECN (3 h) sample shows a smaller semicircle in the small-frequency range, implying a smaller $R_{ct,dl}$ in comparison with MECN, $Co(OH)_2$/MECN (2 h), and $Co(OH)_2$/MECN (4 h). All of the fitted values in EIS are listed in Table 2. The fitted values of $R_{ct,dl}$ are 5.006, 21.91, 4.295, and 6.089 Ω for MECN, $Co(OH)_2$/MECN (2 h), $Co(OH)_2$/MECN (3 h), and $Co(OH)_2$/MECN (4 h), respectively, indicating that $Co(OH)_2$/MECN (3 h) has a faster reaction rate than $Co(OH)_2$/MECN (2 h) and $Co(OH)_2$/MECN (4 h).

Fig. 7(a) compares the cyclic voltammetry (CV) curves of the pristine MECN, $Co(OH)_2$/MECN (2 h), $Co(OH)_2$/MECN (3 h), and $Co(OH)_2$/MECN (4 h) at a scanning rate of 5 mV s^{-1}. At the potential of the HER, the larger current density of $Co(OH)_2$/MECN (3 h) results in higher electrochemical activity arising from the increased surface area and 3D structure. CV was performed on the $Co(OH)_2$/MECN (3 h) in the potential range between −0.35 and 1.65 V *vs.* RHE at scanning rates between 5 and 80 mV s^{-1}. Fig. 7(b) shows the typical curves of the $Co(OH)_2$/MECN (3 h), revealing swift and reversible redox peaks ascribed to more electron/ion paths and faster charge transportation due to the improved conductivity. The $Co(OH)_2$/MECN (3 h) shows two anodic peaks and corresponding cathodic peaks associated with the redox couples of Co^{2+}/Co^{3+} and Co^{3+}/Co^{4+}. As a result, the transition on the surface of $Co(OH)_2$ can be summarized by the following equations:[45]

$$Co(OH)_2 + OH^- \rightarrow CoOOH + H_2O + e^- \quad (5)$$

$$CoOOH + OH^- \rightarrow CoO_2 + H_2O + e^-. \quad (6)$$

Fig. 7(c) presents the polarization curves of the $Co(OH)_2$/MECN (3 h) at different scanning rates between 2 and 10 mV s^{-1}, indicating that the scanning rate has a negligible effect on the HER activity of the $Co(OH)_2$/MECN (3 h). Fig. 7(d) shows the corresponding results at −0.4 V *vs.* RHE. The increase in the cathodic current density of the $Co(OH)_2$/MECN (3 h) can be neglected as the scanning rate increases, indicating the advantages of tetsubo-like $Co(OH)_2$ nanorods with much better stability and electron transfer efficiencies for significantly

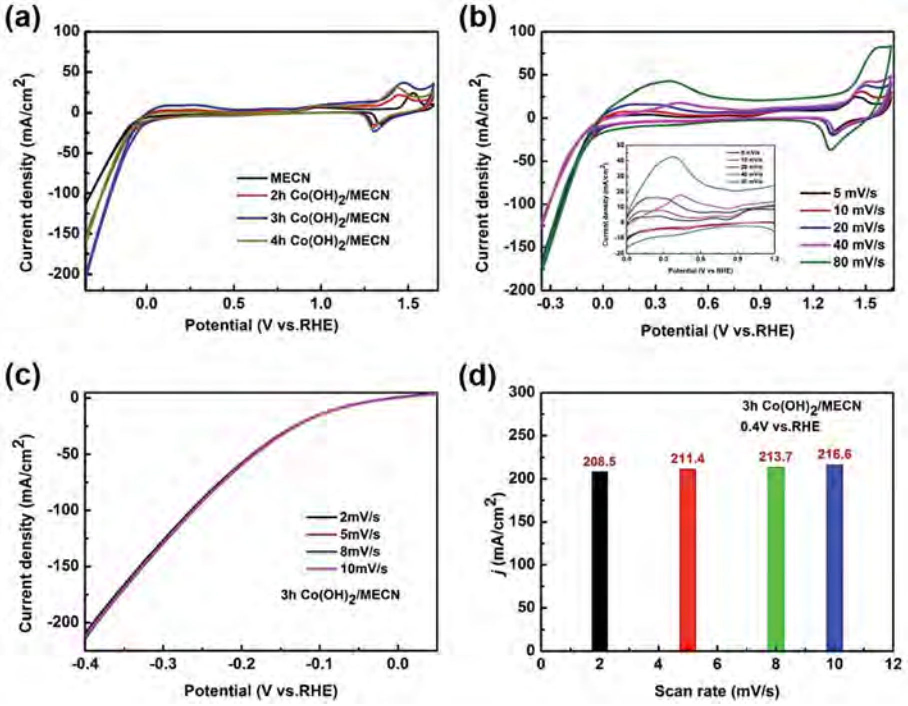

Fig. 7 (a) Cyclic voltammetry curves of MECN, $Co(OH)_2$/MECN (2 h), $Co(OH)_2$/MECN (3 h), and $Co(OH)_2$/MECN (4 h) at a scanning rate of 5 mV s^{-1}; (b) CV curves of $Co(OH)_2$/MECN (3 h) at different scanning rates in 1 M KOH; (c) LSV curves of $Co(OH)_2$/MECN (3 h) at different scanning rates; (d) the corresponding current densities at −0.4 V *vs.* RHE.

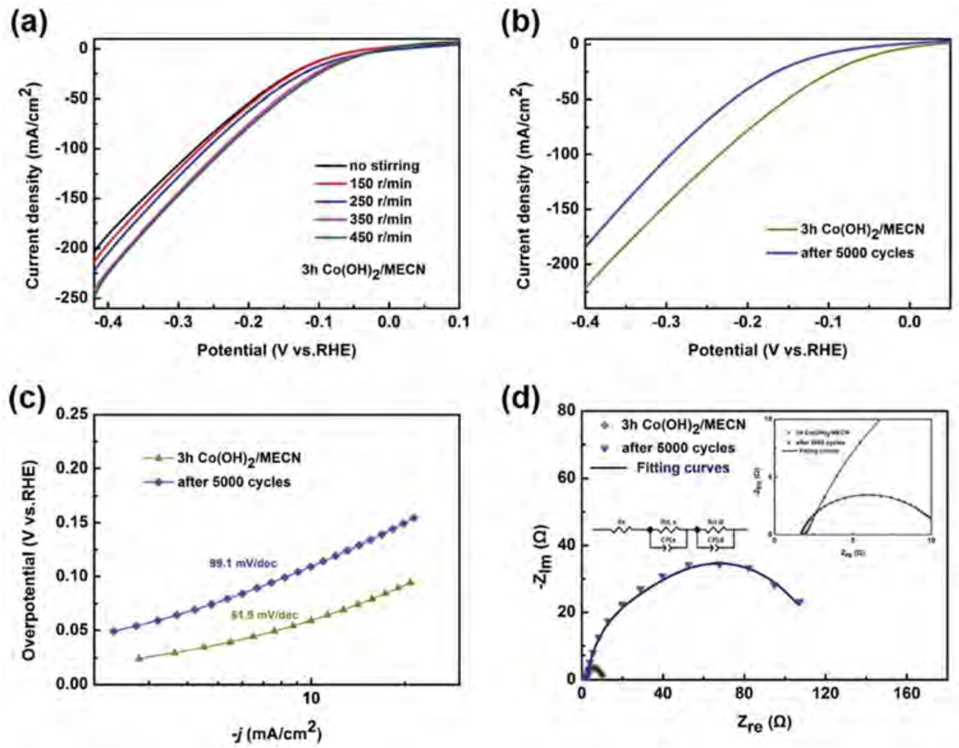

Fig. 8 (a) LSV curves of $Co(OH)_2$/MECN (3 h) at different stirring rates and stability evaluation of $Co(OH)_2$/MECN (3 h) before and after CV; (b) polarization curves; (c) Tafel plots; (d) Nyquist plots.

enhanced HER performance. The tetsubo-like $Co(OH)_2$ nanorods were also believed to facilitate the electron and mass transfer process *via* exposing more active centers to the reactants.

Fig. 8(a) shows the polarization curves of the $Co(OH)_2$/MECN (3 h) at different stirring rates between 0 and 450 rpm. As the stirring speed is increased, the cathodic current density increases at the same potential. Rapid stirring dislodges bubbles, enabling rapid diffusion of electrolyte ions and expediting electron transport. The durability of the $Co(OH)_2$/MECN (3 h) electrocatalyst is evaluated by CV measurement at a scanning rate of 40 mV s^{-1}. The polarization curves of the initial cycle and after 5000 CV cycles are displayed in Fig. 8(b), which shows a mere 40 mA cm^{-2} shift in the current density for the overpotential of −0.4 V *vs.* RHE in the initial 5000 CV cycles. The corresponding Tafel slopes and Nyquist plots in Fig. 8(c) and (d) show that the performance of the $Co(OH)_2$/MECN (3 h) is attenuated to a different degree, partially due to corrosion of the tetsubo-like nanorod structure in the alkaline solution. Nevertheless, these overall results demonstrate the potential application of 3D tetsubo-like $Co(OH)_2$ NRs on MECNs for high-performance energy conversion.

4 Conclusion

Tetsubo-like $Co(OH)_2$ nanorods are fabricated on a 3D macroporous electrically conductive network as efficient electrocatalysts in an alkaline medium. The tetsubo-like $Co(OH)_2$ catalysts were coated on the MECN with a large aspect ratio to form 3D networked nanorods with a large exposed surface area facilitating the electrochemical reactions at the interface between the catalyst and electrolyte. Because of the large surface area, well-separated nanorod structure, uniform growth, and enhanced charge transport, the binder-free tetsubo-like $Co(OH)_2$ NRs/MECN electrode shows excellent HER activity, with a low overpotential of −69.3 mV *vs.* RHE required to deliver a hydrogen production current density of 10 mA cm^{-2}, a Tafel slope of 61.9 mV dec^{-1}, and a high current density (−94.2 mV, 20 mA cm^{-2}) for the HER in 1 M KOH. The synergistic effects between the tetsubo-like $Co(OH)_2$ nanorods and the MECN render the design useful for HER applications.

Acknowledgements

This work was jointly supported by the National Natural Science Foundation of China (No. 61176108), Science and Technology Commission of Shanghai Municipality (No. 14DZ2260800), and City University of Hong Kong Applied Research Grant (ARG) No. 9667122.

References

1 H. Zhang, Z. Ma, J. Duan, H. Liu, G. Liu, T. Wang, K. Chang, M. Li, L. Shi and X. Meng, *ACS Nano*, 2015, **10**, 684–694.
2 X. Zhao, B. M. Sánchez, P. J. Dobson and P. S. Grant, *Nanoscale*, 2011, **3**, 839–855.
3 L. Liao, J. Zhu, X. Bian, L. Zhu, M. D. Scanlon, H. H. Girault and B. Liu, *Adv. Funct. Mater.*, 2013, **23**, 5326–5333.

4 X. Yan, L. Tian, J. Murowchick and X. Chen, *J. Mater. Chem. A*, 2016, **4**, 3683–3688.

5 Z. Huang, Z. Chen, Z. Chen, C. Lv, M. G. Humphrey and C. Zhang, *Nano Energy*, 2014, **9**, 373–382.

6 H. Lin, N. Liu, Z. Shi, Y. Guo, Y. Tang and Q. Gao, *Adv. Funct. Mater.*, 2016, **26**, 5581.

7 W. F. Chen, C. H. Wang, K. Sasaki, N. Marinkovic, W. Xu, J. T. Muckerman, Y. Zhu and R. R. Adzic, *Energy Environ. Sci.*, 2013, **6**, 943–951.

8 X. Yang, A. Y. Lu, Y. Zhu, M. N. Hedhili, S. Min, K. W. Huang, Y. Han and L. J. Li, *Nano Energy*, 2015, **15**, 634–641.

9 J. Deng, P. Ren, D. Deng, L. Yu, F. Yang and X. Bao, *Energy Environ. Sci.*, 2014, **7**, 1919–1923.

10 Z. Yin and F. Chen, *Electrochim. Acta*, 2014, **117**, 84–91.

11 J. N. Sebeelamol and S. M. A. Shibli, *Int. J. Hydrogen Energy*, 2013, **38**, 2271–2282.

12 Y. Hou, J. Li, Z. Wen, S. Cui, C. Yuan and J. Chen, *Nano Energy*, 2015, **12**, 1–8.

13 Y. Wu, G. D. Li, Y. Liu, L. Yang, X. Lian, T. Asefa and X. Zou, *Adv. Funct. Mater.*, 2016, **26**, 4839–4847.

14 C. Ray, S. Dutta, Y. Negishi and T. Pal, *Chem. Commun.*, 2016, **52**, 6095–6098.

15 L. Liao, J. Zhu, X. Bian, L. Zhu, M. D. Scanlon, H. H. Girault and B. Liu, *Adv. Funct. Mater.*, 2013, **23**, 5326–5333.

16 W. F. Chen, J. T. Muckerman and E. Fujita, *Chem. Commun.*, 2013, **44**, 8896–8909.

17 Y. Shi and B. Zhang, *Chem. Soc. Rev.*, 2016, **47**, 1529–1541.

18 A. Sivanantham, P. Ganesan and S. Shanmugam, *Adv. Funct. Mater.*, 2016, **26**, 4661–4672.

19 X. Geng, W. Wu, N. Li, W. Sun, J. Armstrong, A. Al-Hilo, M. Brozak, J. Cui and T. P. Chen, *Adv. Funct. Mater.*, 2014, **24**, 6123–6129.

20 X. Peng, L. Hu, L. Wang, X. Zhang, J. Fu, K. Huo, L. Y. S. Lee, K. Y. Wong and P. K. Chu, *Nano Energy*, 2016, **26**, 603–609.

21 M. C. Weidman, D. V. Esposito, Y. C. Hsu and J. G. Chen, *J. Power Sources*, 2012, **202**, 11–17.

22 C. Daiwon and P. N. Kumta, *J. Am. Ceram. Soc.*, 2007, **90**, 3113–3120.

23 D. H. Youn, S. Han, J. Y. Kim, J. Y. Kim, H. Park, S. H. Choi and J. S. Lee, *ACS Nano*, 2014, **8**, 5164–5173.

24 Z. Zhang, B. Lu, J. Hao, W. Yang and J. Tang, *Chem. Commun.*, 2014, **50**, 11554–11557.

25 P. Liu, J. A. Rodriguez, T. Asakura, A. João Gomes and K. Nakamura, *J. Phys. Chem. B*, 2005, **109**, 4575–4583.

26 Y. Pan, Y. Chen, Y. Lin, P. Cui, K. Sun, Y. Liu and C. Liu, *J. Mater. Chem. A*, 2016, **4**, 14675–14686.

27 X. Yan, L. Tian, M. He and X. Chen, *Nano Lett.*, 2015, **15**, 6015–6021.

28 H. Cheng, Y. Su, P. Y. Kuang, G. F. Chen and Z. Q. Liu, *J. Mater. Chem. A*, 2015, **3**, 19314–19321.

29 C. Bingfei, G. M. Veith, J. C. Neuefeind, R. R. Adzic and P. G. Khalifah, *J. Am. Chem. Soc.*, 2013, **135**, 19186–19192.

30 C. Yuan, X. Zhang, L. Hou, L. Shen, D. Li, F. Zhang, C. Fan and J. Li, *J. Mater. Chem.*, 2010, **20**, 10809–10816.

31 X. Zhou, X. Shen, Z. Xia, Z. Zhang, L. Jing, Y. Ma and Y. Qu, *ACS Appl. Mater. Interfaces*, 2015, **7**, 20322–20331.

32 M. Vidotti, C. V. Greco, E. A. Ponzio and S. I. C. D. Torresi, *Electrochem. Commun.*, 2006, **8**, 554–560.

33 T. Xue, X. Wang and J. M. Lee, *J. Power Sources*, 2012, **201**, 382–386.

34 T. Yoon and K. S. Kim, *Adv. Funct. Mater.*, 2016, **24**, 6123–6129.

35 J. X. Feng, L. X. Ding, S. H. Ye, X. J. He, H. Xu, Y. X. Tong and G. R. Li, *Adv. Mater.*, 2015, **27**, 7051–7057.

36 J. Jiang, A. Zhang, L. Li and L. Ai, *J. Power Sources*, 2015, **278**, 445–451.

37 Z. Li, J. Wang, L. Niu, J. Sun, P. Gong, W. Hong, L. Ma and S. Yang, *J. Power Sources*, 2014, **245**, 224–231.

38 G. Zhang, S. Zang and X. Wang, *ACS Catal.*, 2015, **5**, 941–947.

39 H. Kim, Y. Kim, Y. Noh and W. B. Kim, *Dalton Trans.*, 2016, **45**, 13686–13690.

40 A. D. Jagadale, G. Guan, X. Du, X. Hao, X. Li and A. Abudula, *RSC Adv.*, 2015, **5**, 56942–56948.

41 F. Zheng, G. Mu, Z. Zhang, Y. Shen, M. Zhao and G. Pang, *Mater. Lett.*, 2012, **68**, 453–456.

42 Z. He, Y. Huang and F. He, *RSC Adv.*, 2016, **6**, 15390–15393.

43 M. Li, S. Xu, T. Liu, F. Wang, P. Yang, L. Wang and P. K. Chu, *J. Mater. Chem. A*, 2013, **1**, 532–540.

44 M. Li, S. Xu, C. Cherry, Y. Zhu, D. Wu, C. Zhang, X. Zhang, R. Huang, R. Qi, L. Wang and P. K. Chu, *J. Mater. Chem. A*, 2015, **3**, 13776–13785.

45 M. Li, S. Xu, C. Cherry, Y. Zhu, R. Huang, R. Qi, P. Yang, L. Wang and P. K. Chu, *Electrochim. Acta*, 2014, **149**, 18–27.

46 C. Liang, L. Chen, D. Wu, C. Zhang, S. Xu, Y. Zhu, D. Xiong, P. Yang, L. Wang and P. K. Chu, *Mater. Lett.*, 2016, **172**, 40–43.

47 D. Wu, S. Xu, C. Zhang, Y. Zhu, D. Xiong, R. Huang, R. Qi, L. Wang and P. K. Chu, *J. Mater. Chem. A*, 2016, **4**, 11317–11329.

48 D. Wu, C. Zhang, C. Liang, Y. Zhu, S. Xu, D. Xiong, S. Xue, L. Wang and P. K. Chu, *J. Mater. Chem. C*, 2016, **4**, 2079–2087.

49 D. Wu, S. Xu, M. Li, C. Zhang, Y. Zhu, Y. Xu, W. Zhang, R. Huang, R. Qi and L. Wang, *J. Mater. Chem. A*, 2015, **3**, 16695–16707.

50 L. Ma, Y. Hu, R. Chen, G. Zhu, T. Chen, H. Lv, Y. Wang, J. Liang, H. Liu and C. Yan, *Nano Energy*, 2016, **24**, 139–147.

51 A. B. Laursen, S. Kegnæs, S. Dahl and I. Chorkendorff, *Energy Environ. Sci.*, 2012, **5**, 5577–5591.

52 X. H. Xia, J. P. Tu, Y. Q. Zhang, Y. J. Mai, X. L. Wang, C. D. Gu and X. B. Zhao, *J. Phys. Chem. C*, 2011, **115**, 22662–22668.

53 R. Chen, H. Y. Wang, J. Miao, H. Yang and B. Liu, *Nano Energy*, 2014, **11**, 333–340.

54 L. Mi, W. Wei, S. Huang, S. Cui, W. Zhang, H. Hou and W. Chen, *J. Mater. Chem. A*, 2015, **3**, 20973–20982.

55 C. Xiao, Y. Li, X. Lu and C. Zhao, *Adv. Funct. Mater.*, 2016, **26**, 3515–3523.

56 J. Jiang, J. Liu, R. Ding, J. Zhu, Y. Li, A. Hu, X. Li and X. Huang, *ACS Appl. Mater. Interfaces*, 2011, **3**, 99–103.

57 C. Bingfei, G. M. Veith, J. C. Neuefeind, R. R. Adzic and P. G. Khalifah, *J. Am. Chem. Soc.*, 2013, **135**, 19186–19192.

58 H. Su, H. H. Wang, B. Zhang, K. X. Wang, X. H. Li and J. S. Chen, *Nano Energy*, 2016, **22**, 79–86.

59 J. Tian, Q. Liu, A. M. Asiri and X. Sun, *J. Am. Chem. Soc.*, 2014, **136**, 7587–7590.

60 E. J. Popczun, C. G. Read, C. W. Roske, N. S. Lewis and R. E. Schaak, *Angew. Chem.*, 2014, **126**, 5427–5430.

61 W. J. Zhou, J. Lu, K. Zhou, L. J. Yang, Y. T. Ke, Z. H. Tang and S. W. Chen, *Nano Energy*, 2016, **28**, 143–150.

62 W. Zhou, J. Zhou, Y. Zhou, J. Lu, K. Zhou, L. Yang, Z. Tang, L. Li and S. Chen, *Chem. Mater.*, 2015, **27**, 2026–2032.

63 D. Hou, W. Zhou, K. Zhou, Y. Zhou, J. Zhong, L. Yang, J. Lu, G. Li and S. Chen, *J. Mater. Chem. A*, 2015, **3**, 15962–15968.

64 W. Zhou, Y. Zhou, L. Yang, J. Huang, Y. Ke, K. Zhou, L. Li and S. Chen, *J. Mater. Chem. A*, 2014, **3**, 1915–1919.

65 G. G. Tang, J. R. Sun, C. Wei, K. Q. Wu, X. R. Ji, S. S. Liu, H. Tang and C. S. Li, *Mater. Lett.*, 2012, **86**, 9–12.

66 C. Pacholski, A. Kornowski and H. Weller, *Angew. Chem.*, 2002, **41**, 1188–1191.

67 Y. D. Li, X. L. Li, R. R. He, J. Zhu and Z. X. Deng, *J. Am. Chem. Soc.*, 2002, **124**, 1411–1416.